LETTER

A mechanism of viral immune evasion revealed by cryo–EM analysis of the TAP transporter

Michael L. Oldham[1,2], Richard K. Hite[1,2], Alanna M. Steffen[2], Ermelinda Damko[1], Zongli Li[2,3], Thomas Walz[1] & Jue Chen[1,2]

Cellular immunity against viral infection and tumour cells depends on antigen presentation by major histocompatibility complex class I (MHC I) molecules. Intracellular antigenic peptides are transported into the endoplasmic reticulum by the transporter associated with antigen processing (TAP) and then loaded onto the nascent MHC I molecules, which are exported to the cell surface and present peptides to the immune system[1]. Cytotoxic T lymphocytes recognize non-self peptides and program the infected or malignant cells for apoptosis. Defects in TAP account for immunodeficiency and tumour development. To escape immune surveillance, some viruses have evolved strategies either to downregulate TAP expression or directly inhibit TAP activity. So far, neither the architecture of TAP nor the mechanism of viral inhibition has been elucidated at the structural level. Here we describe the cryo-electron microscopy structure of human TAP in complex with its inhibitor ICP47, a small protein produced by the herpes simplex virus I. Here we show that the 12 transmembrane helices and 2 cytosolic nucleotide-binding domains of the transporter adopt an inward-facing conformation with the two nucleotide-binding domains separated. The viral inhibitor ICP47 forms a long helical hairpin, which plugs the translocation pathway of TAP from the cytoplasmic side. Association of ICP47 precludes substrate binding and prevents nucleotide-binding domain closure necessary for ATP hydrolysis. This work illustrates a striking example of immune evasion by persistent viruses. By blocking viral antigens from entering the endoplasmic reticulum, herpes simplex virus is hidden from cytotoxic T lymphocytes, which may contribute to establishing a lifelong infection in the host.

Inside our body, every nucleated cell has surface 'barcodes' that are surveyed by the immune system. These barcodes are peptides derived from intracellular proteins, presented on the surface by MHC I molecules to indicate whether the cell is healthy (reviewed in ref. 1). Peptides generated from normal cellular proteins are ignored by cytotoxic T cells, whereas viral-derived or malignant peptides will trigger an adaptive immune response, resulting in elimination of the infected or tumour cells. The peptide repertoire is generated in the cytoplasm, mainly by the proteasome, but also in part by cytosolic peptidases (Fig. 1a). Peptide uploading onto MHC I molecules takes place inside the endoplasmic reticulum (ER) and is orchestrated by a macromolecular assembly collectively called the MHC class I peptide-loading complex (PLC). Cytosolic peptides are delivered across the ER membrane by the ATP-binding cassette (ABC) transporter TAP. The chaperones calnexin and calreticulin stabilize nascent MHC I molecules awaiting peptides. The tapasin/ERp57 heterodimer brings MHC I molecules and TAP within close proximity and catalyses peptide loading. Peptide-loaded MHC I molecules are then released from the ER and transported to the cell surface for antigen presentation.

As the MHC I antigen presentation pathway plays a crucial role in eradicating intracellular pathogens, it is not surprising that some viruses have evolved the ability to interfere with this process (reviewed in ref. 2). The peptide transporter TAP in particular is a primary target for viral evasion (reviewed in ref. 3). TAP is a heterodimeric ABC transporter that contains two subunits, TAP1 and TAP2, which share 37% sequence identity and are predicted to have similar structures. Each subunit contains an amino (N)-terminal
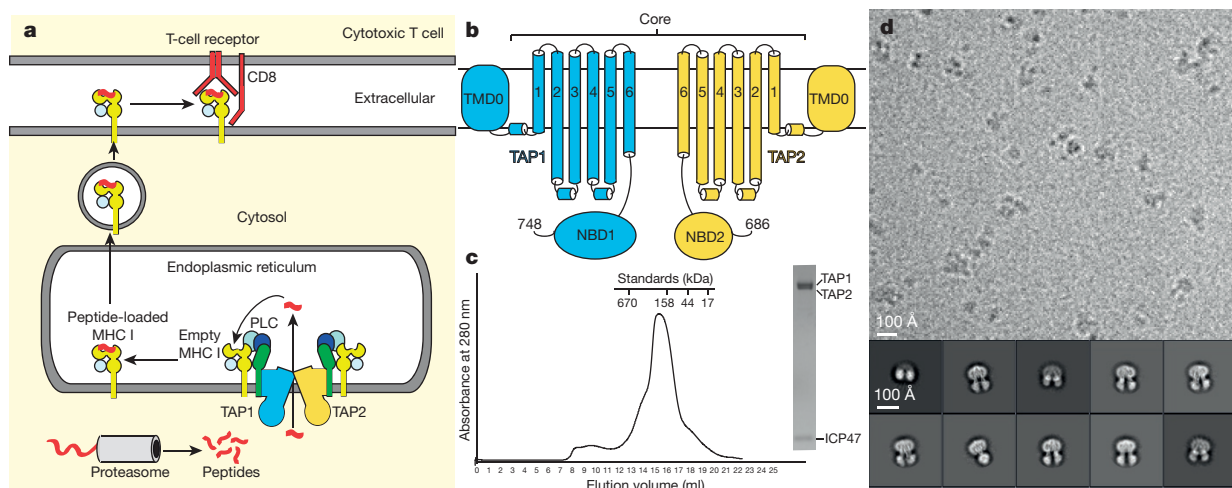

Figure 1 | Purification and cryo-EM characterization of TAP. a, The MHC class I antigen presentation pathway. PLC: peptide-loading complex. **b**, Topology diagram of TAP1 (blue) and TAP2 (gold). The residue numbers of the C termini are indicated. **c**, Gel-filtration profile of the TAP–ICP47 complex. Inset: SDS–polyacrylamide gel electrophoresis of the peak fraction stained with Coomassie blue. **d**, A typical micrograph of the TAP–ICP47 complex after drift correction. Also shown are representative two-dimensional class averages of the particles.

[1]The Rockefeller University, 1230 York Avenue, New York, New York 10065, USA. [2]Howard Hughes Medical Institute, 4000 Jones Bridge Road, Chevy Chase, Maryland 20815, USA. [3]Department of Cell Biology, Harvard Medical School, 240 Longwood Avenue, Boston, Massachusetts 02115, USA.
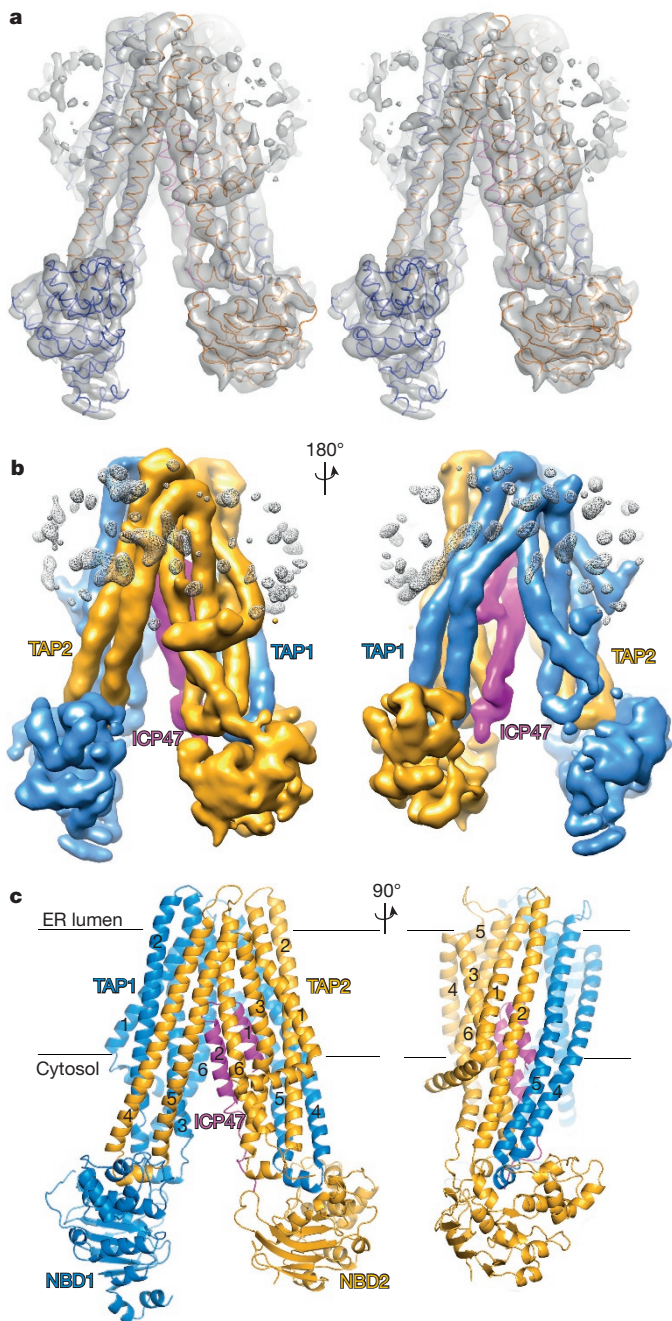
Figure 2 | Three-dimensional reconstruction. a, Stereo view of the overall density map, filtered to 6.5 Å. The α-carbon traces of the TAP core and the N-terminal 50 residues of ICP47 are also shown. **b**, Two views of the overall density map, coloured by protein subunit. **c**, Ribbon diagram of the poly-alanine model presented in two orthogonal views. The TM helices in the core of the transporter are labelled according to Fig. 1b. TAP1, blue; TAP2, gold; ICP47, magenta.

transmembrane region (TMD0) that interacts with tapasin, followed by six transmembrane (TM) helices that form the peptide translocation pathway and a canonical nucleotide-binding domain (NBD) that hydrolyses ATP (Fig. 1b)[4]. The core TAP, devoid of the TMD0s, is necessary and sufficient for peptide transport[4]. So far, five viral proteins have been identified as TAP inhibitors. Four are encoded by members of the herpes virus family and one by cowpox virus[3]. These viral inhibitors are valuable tools for selective immune suppression and for understanding the fundamental mechanism of antigen presentation.
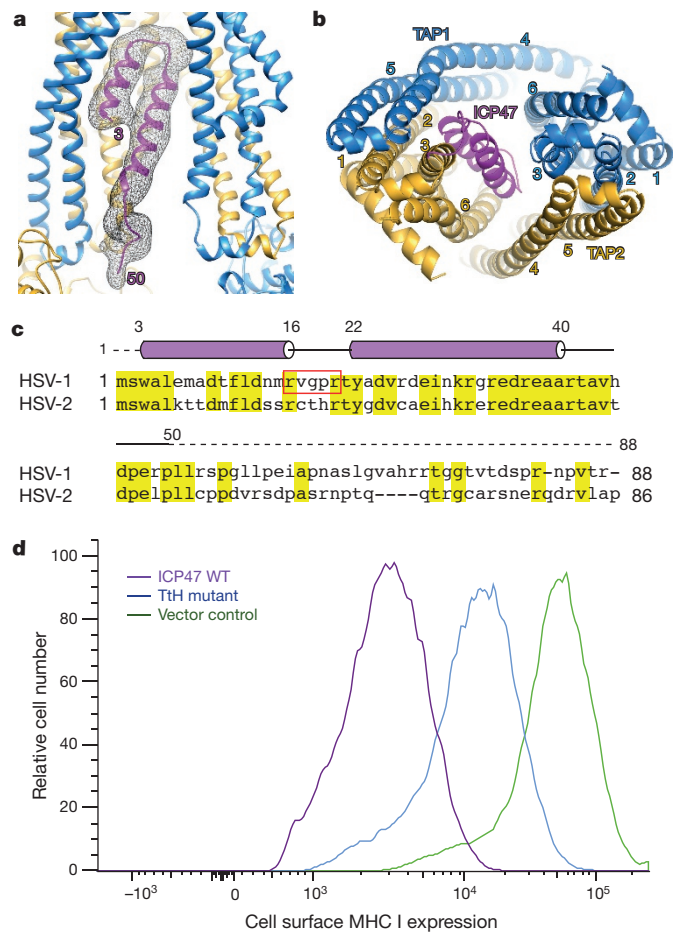

Figure 3 | The viral inhibitor ICP47 plugs into the transmembrane pathway. a, EM density corresponding to ICP47 (black mesh), viewed from the plane of the membrane. Terminal residues in the ICP47 model are indicated. **b**, Binding of ICP47 to TAP, viewed along the membrane normal from the cytoplasm. **c**, The helix–loop–helix structure of ICP47 is conserved between HSV-1 and HSV-2. Conserved residues are highlighted in yellow. A red box highlights residues replaced by alanine in the 'turn-to-helix' (TtH) mutant. **d**, FACS analysis (three repeats) of MHC I surface expression in cells expressing wild-type (WT) and mutant ICP47.

Here we focus our study on a TAP inhibitor encoded by herpes simplex virus (HSV). Both types of HSV, HSV-1 (oral herpes) and HSV-2 (genital herpes), somehow elude the human immune system and lead to a lifelong infection. The first clue as to how HSV bypasses the immune system came from observations that cells infected by HSV have reduced surface expression of MHC I molecules[5] and are resistant to cytotoxic T cells[6]. Since this resistance develops within 3 hours of HSV infection, researchers narrowed their search for the responsible gene to those few expressed in the early stage of infection[7,8]. Out of these, an 88-residue protein, ICP47, was found to bind to TAP and prevent peptide translocation into the ER[7,8]. Consequently, empty MHC I molecules were retained in the ER and viral peptide presentation was suppressed. Subsequent studies have shown that ICP47 interacts with TAP from the cytosolic side of the membrane and somehow prevents peptide binding[9,10]. The functional domain of ICP47 has been mapped to the N-terminal 35 residues[11,12], which form an extended helix–loop–helix structure in lipid bilayers[13].

In this study, we pursued structural determination of a TAP–ICP47 complex using cryo-electron microscopy (cryo-EM). The small size of the complex (166 kDa total) and the predicted pseudo-twofold symmetry between TAP1 and TAP2 make it extremely challenging to accurately align particles for three-dimensional reconstruction. To maximize the difference between the two TAP subunits, we used
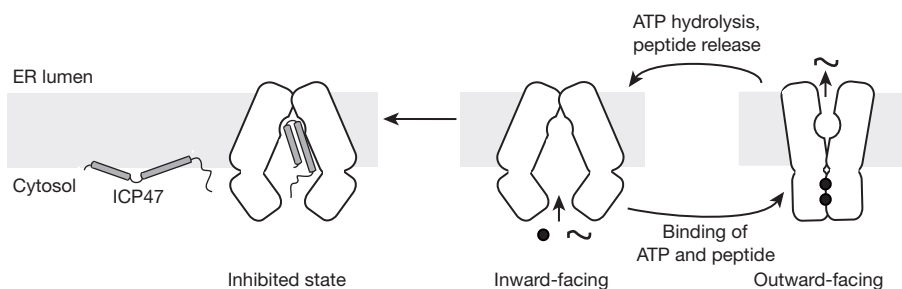
Figure 4 | ICP47 precludes peptide binding and traps TAP in an inward-facing conformation. TAP functions via alternating access, cycling between two major conformations (right). In the absence of substrates, the transporter rests in an inward-facing state in which the two NBDs are separated and the translocation pathway is exposed to the cytosol. Upon association of substrates and ATP, the transporter undergoes a conformational change that reorients the TMDs and positions ATP at a closed NBD dimer interface for hydrolysis. ATP hydrolysis releases the substrate and resets the transporter to the resting state. ICP47 binds TAP stabilizing the inward-facing conformation (left).

a shorter allele of TAP2 that lacks the last 17 amino acids in NBD2 (Fig. 1b)[14]. Co-expression of TAP1 and TAP2 in *Pichia pastoris* (Extended Data Fig. 1) produced a heterodimer that dissociates readily in detergents. However, by incubating the TAP-enriched membranes with ICP47 before detergent solubilization, the complex consisting of TAP1, TAP2, and ICP47 becomes more stable (Fig. 1c, d). Cryo-EM analysis of this complex (Extended Data Fig. 2 and Fig. 1d) produced a density map (Fig. 2) of an overall resolution of 6.5 Å, determined by the gold-standard refinement procedure (Extended Data Fig. 3)[15]. In this reconstruction the TM helices and the connectivity between the helices are clearly resolved. The density corresponding to one NBD is significantly smaller than that for the other, allowing us to confidently differentiate TAP1 from TAP2 (Fig. 2b). Most importantly, we observe strong density corresponding to the functional region of ICP47, which reveals how this viral protein inhibits peptide translocation (Fig. 2b).

The core region of TAP adopts an inverted 'V'-shaped structure, with the two TMDs making close contact on the side corresponding to the ER lumen and the NBDs separated from each other inside the cytosol (Fig. 2c). Domain swapping of TM helices 4 and 5 across the TAP1/TAP2 interface is a prominent structural feature (Fig. 2c). Indeed, the overall structure of TAP is very similar to that of other ABC exporters, including the lipid flippase MsbA from Gram-negative bacteria[16], the protein transporter PCAT1 from Gram-positive bacteria[17], and the multidrug transporter P-glycoprotein in eukaryotes[18,19]. Although these transporters recognize very different substrates, they must share a common evolutionary origin and a common mechanism for coupling ATP hydrolysis to substrate translocation.

No density was observed for the N-terminal TMD0 domain of both TAP1 and TAP2 subunits (Fig. 2). Studies have shown that the TMD0s are essential to the assembly of the large peptide-loading complex[4,20] but dispensable in peptide translocation[4]. ICP47 inhibits both full-length TAP and the core construct[4]. Our results indicate that in the absence of tapasin the two TMD0s are flexibly tethered to the core region of TAP.

Biochemical data and homology modelling suggest that the peptide translocation pathway lies at the interface of the two TMDs[21,22]. Inside this pathway, we observe strong density consistent with the helix–loop–helix structure of ICP47 (Figs 2b and 3a). Guided by the NMR structure and secondary structure prediction[13], we built residues 3–16 into the shorter helical density and residues 22–40 into the longer density (Fig. 3). Additional density is packed along the cytosolic region of TAP2, into which we modelled residues 41–50. The carboxy (C)-terminal region, neither required for TAP inhibition nor conserved between HSV-1 and HSV-2 (Fig. 3c), is not resolved in the EM map, suggesting high mobility.

On the basis of this model, the N-terminal half of ICP47 forms a hairpin-like structure pinned against the inner surface of TAP2 TM helices 2, 3, 6 and TAP1 TM helix 4 (Fig. 3b). The two helices of ICP47 run anti-parallel to each other, connected by a sharp turn at the top of the TM cavity. The extensive packing between TAP and ICP47 is

consistent with the nanomolar affinity of ICP47, orders of magnitude higher than those of the substrate peptides[9,12].

The potency of ICP47 appears to come from its helical hairpin structure, which provides a greater interface with TAP than a typical substrate. To test whether the flexibility of the connecting loop is important, we constructed a 'turn-to-helix' mutant by replacing residues 16–22 with alanine, which has the highest propensity to form an α-helix and thus would oppose (but not preclude) the formation of a turn. ICP47 activity was measured in human epithelial cells, in which cytosolic expression of ICP47 inhibits endogenous TAP and reduces the amount of MHC I molecules expressed on the cell surface. A green fluorescent protein (GFP) tag was fused to the C terminus of ICP47 as a marker to select for cells expressing similar amounts of ICP47. Consistent with the EM structure and previous mutagenesis data[11], the 'turn-to-helix' mutant is much less potent than the wild-type construct. Specifically, mutant ICP47 reduced surface MHC I expression by only fivefold as opposed to a 20-fold reduction by wild-type ICP47 (Fig. 3d).

Although ICP47 competes for the same binding site, we do not believe it mimics the substrate binding process. Unlike substrates, ICP47 inhibits rather than stimulates ATP hydrolysis[23]. Furthermore, in contrast to ICP47, which separates the two NBDs, substrate binding induces partial closure of the NBDs[24]. More recently, electron paramagnetic resonance studies showed that TAP binds its substrates in their extended conformations, comparable to how MHC I molecules present peptides[25].

Comparison of our structure with the NMR structure of ICP47 (ref. 13) suggests that it undergoes major conformational changes upon association with TAP (Fig. 4). In isolation, the N-terminal two helices of ICP47 are flexibly linked and bind to the surface of the membrane at a slight tilt[13]. In the complex with TAP, ICP47 forms a straight hairpin and inserts perpendicularly into the membrane. Although exact determinations of the amino acid register cannot be made at the current resolution, the overall structure readily explains how ICP47 inhibits peptide transport into the ER. By plugging a long helical hairpin into the translocation pathway, ICP47 directly blocks substrates from binding. Furthermore, because ICP47 is too large to be transported by TAP, its high-affinity binding traps TAP in an inactive conformation. Like other ABC transporters, TAP functions by alternating between two major conformations, each exposing the translocation pathway to one side of the membrane (Fig. 4). Binding of ICP47 stabilizes the inward-facing conformation, and thus prevents TAP from transitioning to an outward-facing state in which the NBDs form a closed dimer and the translocation pathway orientates towards the ER lumen (Fig. 4).

In addition to viral inhibition discussed in this study, the structural basis of two cellular regulatory mechanisms has been elucidated[26–28]; both are relevant to nutrient uptake in bacteria. As a classic example of carbon catabolite repression, when a preferred carbon source is available, bacteria suppress the uptake of maltose through direct binding of a regulatory protein to the maltose transporter[26]. Methionine

and molybdate transporters offer another example[27,28]. In both cases, at high intracellular concentration, the substrate binds and inhibits the corresponding transporter, a feedback mechanism that limits the amount of import into the cell[27,28]. Unlike viral inhibition, both cellular inhibitions are allosteric and reversible, regulated by the metabolic state of the cells. One common theme among all these inhibition mechanisms is that the inhibitor binds and stabilizes the transporter in the inward-facing state, a conformation unable to hydrolyse ATP. We speculate that this strategy may be advantageous in preserving cellular energy sources. It is also possible that for most ABC transporters, the inward-facing state is most common and thus naturally targeted by regulators.

Online Content Methods, along with any additional Extended Data display items and Source Data, are available in the online version of the paper; references unique to these sections appear only in the online paper.

1. Blum, J. S., Wearsch, P. A. & Cresswell, P. Pathways of antigen processing. *Annu. Rev. Immunol.* **31,** 443–473 (2013).
2. van de Weijer, M. L., Luteijn, R. D. & Wiertz, E. J. Viral immune evasion: lessons in MHC class I antigen presentation. *Semin. Immunol.* **27,** 125–137 (2015).
3. Verweij, M. C. *et al.* Viral inhibition of the transporter associated with antigen processing (TAP): a striking example of functional convergent evolution. *PLoS Pathog.* **11,** e1004743 (2015).
4. Koch, J., Guntrum, R., Heintke, S., Kyritsis, C. & Tampé, R. Functional dissection of the transmembrane domains of the transporter associated with antigen processing (TAP). *J. Biol. Chem.* **279,** 10142–10147 (2004).
5. Hill, A. B., Barnett, B. C., McMichael, A. J. & McGeoch, D. J. HLA class I molecules are not transported to the cell surface in cells infected with herpes simplex virus types 1 and 2. *J. Immunol.* **152,** 2736–2741 (1994).
6. York, I. A. *et al.* A cytosolic herpes simplex virus protein inhibits antigen presentation to CD8+ T lymphocytes. *Cell* **77,** 525–535 (1994).
7. Hill, A. *et al.* Herpes simplex virus turns off the TAP to evade host immunity. *Nature* **375,** 411–415 (1995).
8. Früh, K. *et al.* A viral inhibitor of peptide transporters for antigen presentation. *Nature* **375,** 415–418 (1995).
9. Tomazin, R. *et al.* Stable binding of the herpes simplex virus ICP47 protein to the peptide binding site of TAP. *EMBO J.* **15,** 3256–3266 (1996).
10. Ahn, K. *et al.* Molecular mechanism and species specificity of TAP inhibition by herpes simplex virus ICP47. *EMBO J.* **15,** 3247–3255 (1996).
11. Galocha, B. *et al.* The active site of ICP47, a herpes simplex virus-encoded inhibitor of the major histocompatibility complex (MHC)-encoded peptide transporter associated with antigen processing (TAP), maps to the NH2-terminal 35 residues. *J. Exp. Med.* **185,** 1565–1572 (1997).
12. Neumann, L., Kraas, W., Uebel, S., Jung, G. & Tampé, R. The active domain of the herpes simplex virus protein ICP47: a potent inhibitor of the transporter associated with antigen processing. *J. Mol. Biol.* **272,** 484–492 (1997).
13. Aisenbrey, C. *et al.* Structure and dynamics of membrane-associated ICP47, a viral inhibitor of the MHC I antigen-processing machinery. *J. Biol. Chem.* **281,** 30365–30372 (2006).
14. Powis, S. H. *et al.* Polymorphism in a second ABC transporter gene located within the class II region of the human major histocompatibility complex. *Proc. Natl Acad. Sci. USA* **89,** 1463–1467 (1992).
15. Henderson, R. *et al.* Outcome of the first electron microscopy validation task force meeting. *Structure* **20,** 205–214 (2012).
16. Ward, A., Reyes, C. L., Yu, J., Roth, C. B. & Chang, G. Flexibility in the ABC transporter MsbA: alternating access with a twist. *Proc. Natl Acad. Sci. USA* **104,** 19005–19010 (2007).
17. Lin, D. Y., Huang, S. & Chen, J. Crystal structures of a polypeptide processing and secretion transporter. *Nature* **523,** 425–430 (2015).
18. Aller, S. G. *et al.* Structure of P-glycoprotein reveals a molecular basis for poly-specific drug binding. *Science* **323,** 1718–1722 (2009).
19. Jin, M. S., Oldham, M. L., Zhang, Q. & Chen, J. Crystal structure of the multidrug transporter P-glycoprotein from *Caenorhabditis elegans*. *Nature* **490,** 566–569 (2012).
20. Leonhardt, R. M., Keusekotten, K., Bekpen, C. & Knittler, M. R. Critical role for the tapasin-docking site of TAP2 in the functional integrity of the MHC class I-peptide-loading complex. *J. Immunol.* **175,** 5104–5114 (2005).
21. Nijenhuis, M. & Hämmerling, G. J. Multiple regions of the transporter associated with antigen processing (TAP) contribute to its peptide binding site. *J. Immunol.* **157,** 5467–5477 (1996).
22. Corradi, V., Singh, G. & Tieleman, D. P. The human transporter associated with antigen processing: molecular models to describe peptide binding competent states. *J. Biol. Chem.* **287,** 28099–28111 (2012).
23. Gorbulev, S., Abele, R. & Tampé, R. Allosteric crosstalk between peptide-binding, transport, and ATP hydrolysis of the ABC transporter TAP. *Proc. Natl Acad. Sci. USA* **98,** 3732–3737 (2001).
24. Geng, J., Sivaramakrishnan, S. & Raghavan, M. Analyses of conformational states of the transporter associated with antigen processing (TAP) protein in a native cellular membrane environment. *J. Biol. Chem.* **288,** 37039–37047 (2013).
25. Herget, M. *et al.* Conformation of peptides bound to the transporter associated with antigen processing (TAP). *Proc. Natl Acad. Sci. USA* **108,** 1349–1354 (2011).
26. Chen, S., Oldham, M. L., Davidson, A. L. & Chen, J. Carbon catabolite repression of the maltose transporter revealed by X-ray crystallography. *Nature* **499,** 364–368 (2013).
27. Kadaba, N. S., Kaiser, J. T., Johnson, E., Lee, A. & Rees, D. C. The high-affinity *E. coli* methionine ABC transporter: structure and allosteric regulation. *Science* **321,** 250–253 (2008).
28. Gerber, S., Comellas-Bigler, M., Goetz, B. A. & Locher, K. P. Structural basis of trans-inhibition in a molybdate/tungstate ABC transporter. *Science* **321,** 246–250 (2008).

Author Contributions M.L.O. performed protein purification and cryo-EM experiments. R.K.H. provided guidance in data processing. A.M.S. provided assistance with protein expression and purification. E.D. performed the fluorescence-activated cell sorting (FACS) experiments. Z.L. and T.W. collected preliminary cryo-EM data and generated the initial model. M.L.O. and J.C. prepared the manuscript with input from all co-authors.

Author Information The three-dimensional cryo-EM density map has been deposited in the Electron Microscopy Data Bank under the accession number EMD-6533. Reprints and permissions information is available at www.nature.com/reprints. The authors declare no competing financial interests. Readers are welcome to comment on the online version of the paper. Correspondence and requests for materials should be addressed to J.C. (juechen@rockefeller.edu).

METHODS

No statistical methods were used to predetermine sample size. The experiments were not randomized. The investigators were not blinded to allocation during experiments and outcome assessment.

Expression and purification of ICP47. The gene encoding human herpes simplex virus 1 (HSV-1) ICP47 was synthesized (BioBasic) and subcloned into the ligation-independent cloning vector pMCSG20 (Amp[R]), which contained an N-terminal glutathione S-transferase (GST) affinity tag preceding a tobacco etch virus (TEV) protease cleavage site. BL21(DE3)RIL *Escherichia coli* cells containing the pMCSG20-ICP47 vector were grown to mid-exponential phase at 37 °C in Lysogeny broth (LB) medium and expression was induced with 200 μM isopropyl β-D-thiogalactoside (IPTG) at 20 °C for 24 h. The cells were harvested via centrifugation (4,000g for 12 min at 4 °C) and broken by two passes through a high-pressure homogenizer (EmulsiFlex-C3; Avestin). Cell lysate supernatants were loaded onto glutathione sepharose 4B resin (GE Healthcare) equilibrated with PBS buffer, pH 7.4, containing 5 mM D,L-dithiothreitol (DTT). To remove the GST tag from ICP47, the column was equilibrated into a TEV protease cleavage buffer containing 50 mM Tris-HCl, pH 8.0, 200 mM NaCl, 0.5 mM EDTA, and 5 mM DTT and incubated with TEV protease overnight. Untagged ICP47 was eluted and further purified by Superdex 75 gel-filtration chromatography (GE Healthcare) in TEV-cleavage buffer. Fractions containing the protein were pooled, concentrated to 3 mg ml^{-1}, and flash-frozen in liquid nitrogen.

Co-expression of TAP1/TAP2. Synthetic human *TAP1* and *TAP2* genes were codon-optimized for expression in *P. pastoris* (BioBasic) and subcloned into pPICZ-C-XE-protein A (Zeo[R]) and pPICZ-C-XE vectors (Zeo[R]), respectively. To ensure co-expression at a 1:1 molar ratio, we took advantage of the compatible cohesive ends of BamHI and BglII restriction sites to generate an expression cassette as outlined in Extended Data Fig. 1. The resultant vector was linearized by PmeI digestion and transformed into a HIS$^+$ strain of SMD1163 by electroporation (BioRad Gene Pulser II). Transformants were selected on yeast extract peptone dextrose sorbitol (YPDS) agar containing 800 μg ml^{-1} zeocin. Colonies were grown in yeast extract peptone dextrose (YPD) cultures at 28 °C until they reached an absorbance at 600 nm, $A_{600\,nm}$, of 4 to seed flasks containing minimal glycerol medium (MGY), 13.4% yeast nitrogen base, and 1% glycerol at a starting $A_{600\,nm}$ of 0.5. The MGY cultures were grown at 28 °C for 24 h until they reached an $A_{600\,nm}$ of 20, at which point they were harvested by centrifugation (1,500g for 15 min at 4 °C) and used to seed flasks containing minimal methanol medium (MMY), 13.4% yeast nitrogen base, and 0.5% methanol at a starting $A_{600\,nm}$ of 10. These MMY cultures were grown at 28 °C for 24 h before harvesting (1,500g for 15 min at 4 °C). Cell pellets were fractionated and flash-frozen in liquid nitrogen.

Purification of the TAP–ICP47 complex. Cells expressing TAP1-protein A/TAP2 were lysed using a mixer mill (Retsch Mixer Mill 400) and incubated with purified ICP47 in a buffer containing 50 mM Tris-HCl, pH 8, 500 mM NaCl, 15% glycerol, DNase I, protease inhibitors, and 2 mM TCEP for 30 min. Cells were then solubilized with 1.5% n-dodecyl-β-D-maltoside (DDM; Anatrace) for 2 h. The solubilized fraction was isolated by centrifugation (70,000g for 40 min at 4 °C). The TAP1-protein A/TAP2/ICP47 complex was isolated using the protein A affinity tag on TAP1 by IgG Sepharose 6 Fast Flow (GE Healthcare). After extensive washing, PreScission protease (GE Healthcare) was added to the column and incubated overnight to remove the protein A tag. The complex was eluted with additional buffer and further purified using a Superose 6 column (GE Healthcare) equilibrated with 20 mM HEPES, pH 7.4, 150 mM NaCl, 2 mM TCEP, 1 mM DDM, and 1 mM octaethylene glycol monododecyl ether (C12E8; Anatrace). The peak fraction was used to prepare cryo-EM grids.

Initial cryo-EM imaging and generation of an initial model. Vitrified specimens of TAP–ICP47 complex were prepared on glow-discharged Quantifoil holey carbon grids by plunge-freezing into liquid ethane using a Vitrobot (FEI). Cryo-EM data were collected at liquid-nitrogen temperature using a K2 Summit direct electron detector camera (Gatan) on a Tecnai F20 electron microscope (FEI) operating at 200 keV. Dose-fractionated image stacks were recorded with UCSF Image 4 (ref. 29) in super-resolution counting mode at a calibrated magnification of ×40,410 (nominal magnification of ×29,000) with a dose rate of 8 electrons per pixel per second (5.2 electrons per square ångström per second). Frames were read out every 200 ms and 30 frames were collected, resulting in an exposure time of 6 s and a total dose of 31.2 electrons per square ångström. Dose-fractionated image stacks were twice binned and motion-corrected, as described[29]. The defocus was determined with CTER[30]. BOXER was used to interactively pick 28,813 particles from ~750 images[31]. The particle images were subjected to the iterative stable alignment and clustering (ISAC) procedure[32] implemented in SPARX[33]. Four ISAC generations specifying 100 particles per group and a pixel error threshold of 0.7 yielded 324 averages. Of these,

270 averages were used to calculate an initial three-dimensional density map with the validation of individual parameter reproducibility (VIPER) procedure in SPARX.

EM sample preparation and imaging for the final three-dimensional reconstruction. Cryo-EM grids were prepared by pipetting 3 μl freshly purified TAP–ICP47 (2 mg ml^{-1}) onto glow-discharged C-flat holey carbon CF-1.2/1.3-4C grids (Protochips) and letting the sample adsorb for 20 s. The grids were blotted for 4 s at 90% humidity using a Vitrobot Mark IV (FEI) and immediately plunge-frozen in liquid-nitrogen-cooled liquid ethane. The grids were imaged using a FEI Titan Krios electron microscope operating at an acceleration voltage of 300 keV. Images were recorded using a K2 Summit direct electron detector (Gatan) set to super-resolution counting mode with a super-resolution pixel size of 0.675 Å using the program SerialEM[34]. In addition, a Gatan Imaging filter with a slit width of 20 eV was used to remove inelastically scattered electrons. Movie frames were recorded with an exposure time of 200 ms using a dose rate of 10 electrons per pixel per second or 5.5 electrons per square ångström per second (1.35 Å at the image plane). Three data sets were recorded using different total doses and defocus ranges (Extended Data Table 1 and Extended Data Fig. 2).
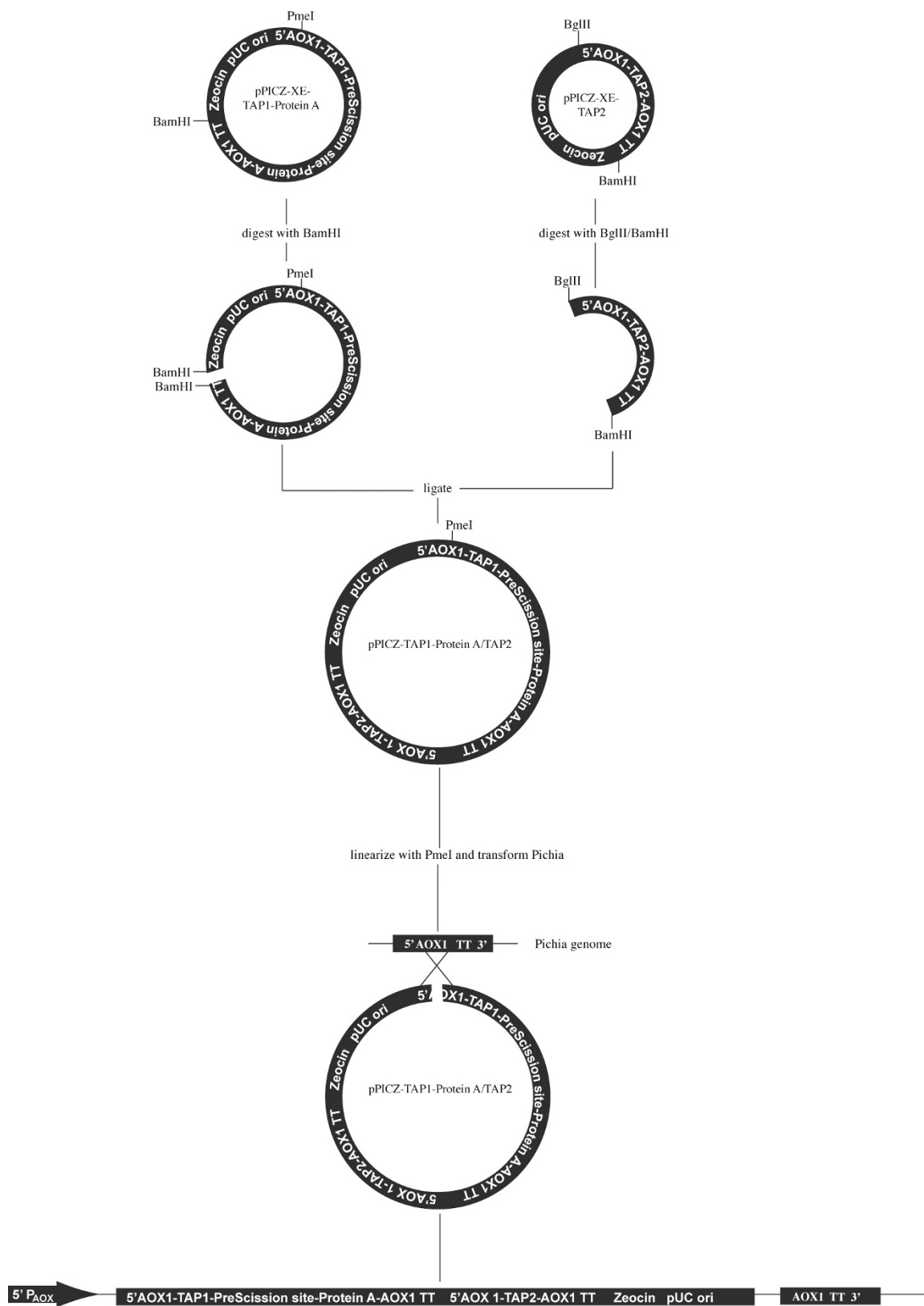
Image processing. Movie frames were corrected for gain reference and binned by a factor of 2, giving a pixel size of 1.35 Å. Drift correction was performed using the program Unblur[35,36]. Next, the drift-corrected frames were summed into single micrographs, which were used to estimate the contrast transfer function (CTF) using CTFFIND4[37]. The program Summovie was used to recalculate the summed images, first with a low-pass filter for autopicking and then with the noise power restored after filtering for particle extraction[38]. Autopicking, particle extraction, two-dimensional classification, three-dimensional classification, and initial three-dimensional refining were all performed in Relion[39]. To achieve a more robust classification of the extracted particles, two-dimensional classification was performed with a particle mask diameter of 145 Å while ignoring the effects of the CTF until the first zero transition. Three-dimensional classification was performed on particles from selected two-dimensional classes using the initial model calculated in SPARX as a reference map. Particles from selected three-dimensional classes from both data sets were combined for three-dimensional refinement. Using the orientation parameters determined by Relion, three-dimensional refinement in FREALIGN was also performed[40]. The final map, reconstructed from 139,293 particles, had a resolution of 6.5 Å as determined by Fourier shell correlation (FSC) of independently refined half-data sets using the 0.143 cut-off criterion (Extended Data Fig. 3).

Model building. We used a model of the TAP1 NBD from a previously reported structure of the isolated domain (PDB accession number 1JJ7)[41] to generate a homology model for the TAP2 NBD using the program Modeller[42]. We also generated a homology model of the TAP1 and TAP2 TMDs using the half-transporter subunit of human ABCB10 (PDB accession number 4AYT) as the source structure[43]. We manually docked these poly-alanine models into our final cryo-EM map and rebuilt each model in Coot[44].
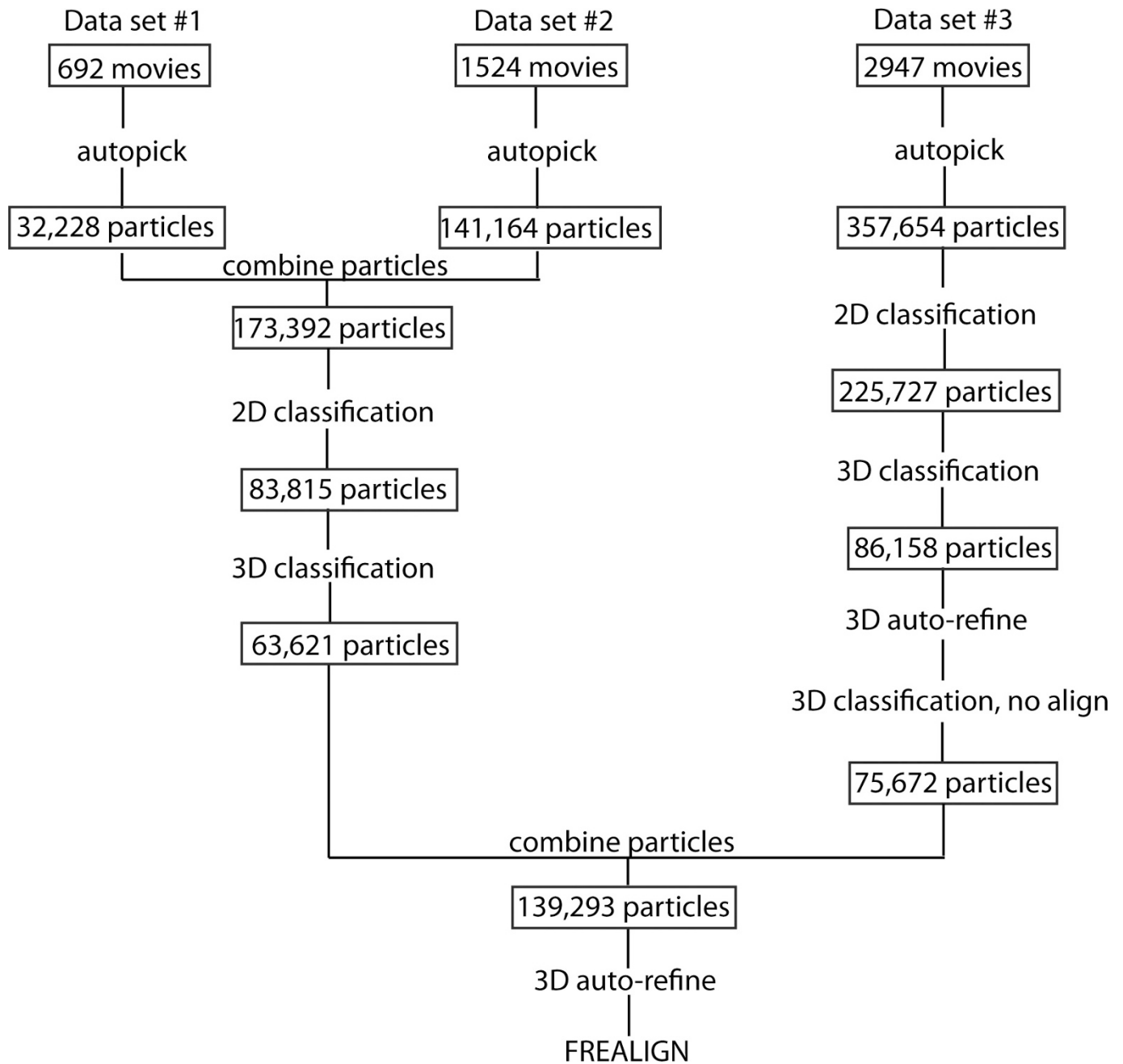
Flow cytometry analysis of MHC I surface expression. MHC I surface expression was analysed using the phycoerythrin-coupled antibody W6/32 (Abcam), which recognizes a monomorphic epitope shared among MHC class I molecules. Genes encoding HSV-1 wild-type ICP47 and the 'turn-to-helix' (TtH) mutant were cloned into a modified version of the pCDNA 3.1 vector (Life Technologies) that added a C-terminal enhanced GFP tag. HeLa cells (ATCC CCL-2) were seeded in six-well plates at a density of 5×10^5 cells per well and transfected with wild-type ICP47, the TtH mutant, or the empty vector. Cells were detached from the plate using trypsin-EDTA (0.05%) at 72 h after transfection and washed in ice-cold FACS buffer (Ca^{2+}/Mg^{2+}-free phosphate buffer, 10% FCS, 1% sodium azide) and centrifuged at 400g for 5 min at 4 °C. Non-specific binding was blocked by incubating the cells with phosphate buffer containing 5% (w/v) bovine serum albumin (BSA) for 15 min on ice. Antibody was added at 5 μg ml^{-1} and incubated for 30 min at 4 °C in the dark. Subsequently, the cells were washed three times in FACS buffer, resuspended at a density of 3×106 cells per millilitre, and counted using a BD LSR II Flow Cytometer (BD Biosciences). The cells were analysed at wavelengths 405 nm for DAPI nuclear stain, 488 nm for GFP fluorescence, and 561 nm for phycoerythrin fluorescence. Only live, single cells with the same levels of GFP fluorescence were used in phycoerythrin gating to compare MHC class I expression. The flow cytometry data were analysed using FlowJo 10.1 single cell analysis software (Tree Star). All experiments were repeated three times. The cell line was tested for mycoplasma contamination by PCR using a Universal Mycoplasma Detection Kit (ATCC 30-1012K).

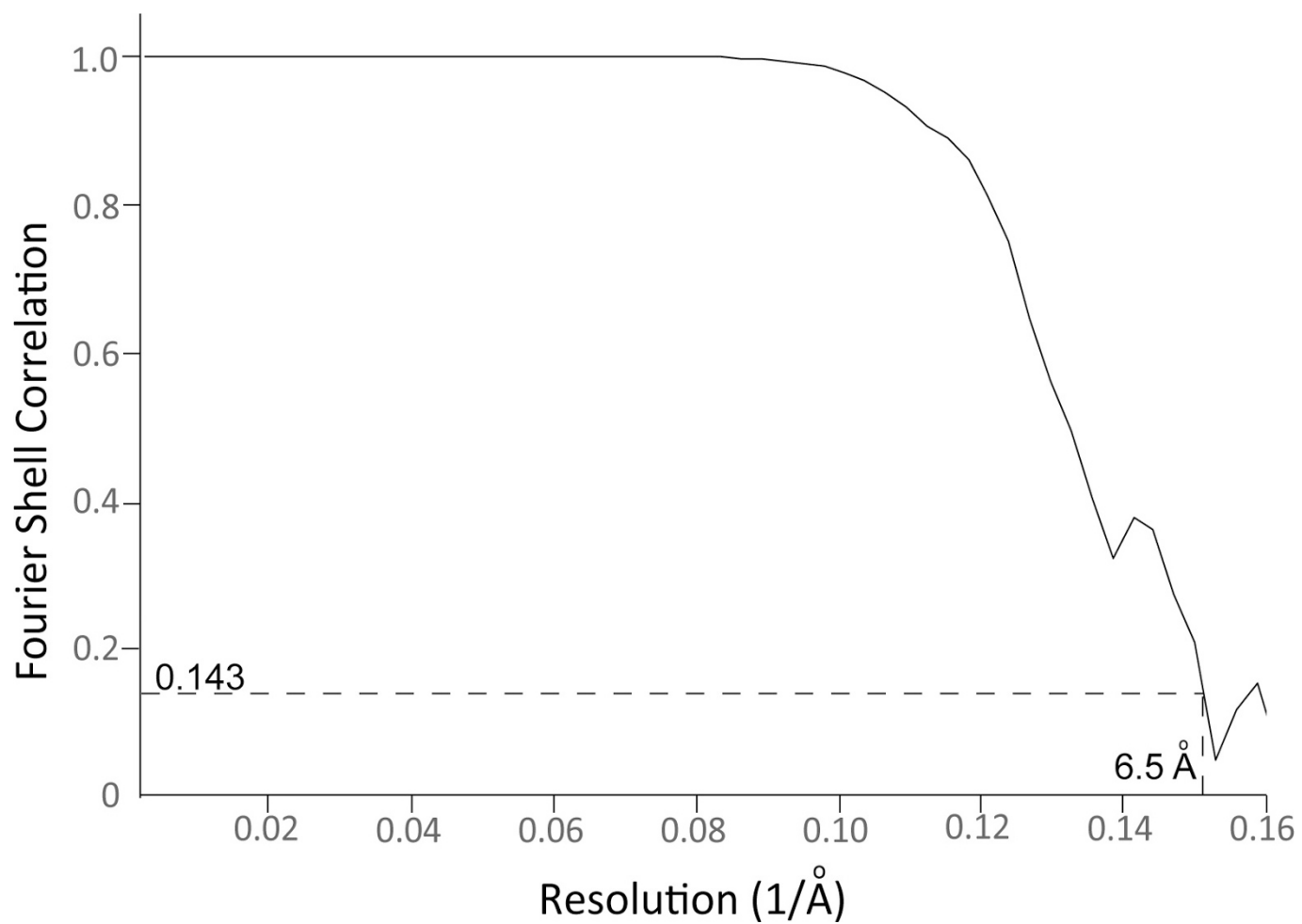**Figure preparation.** Figures were prepared using the programs PyMOL[45], Chimera[46], and FlowJo 10.1.

29. Li, X. *et al.* Electron counting and beam-induced motion correction enable near-atomic-resolution single-particle cryo-EM. *Nature Methods* **10,** 584–590 (2013).
30. Penczek, P. A. *et al.* CTER-rapid estimation of CTF parameters with error assessment. *Ultramicroscopy* **140,** 9–19 (2014).
31. Ludtke, S. J., Baldwin, P. R. & Chiu, W. EMAN: semiautomated software for high-resolution single-particle reconstructions. *J. Struct. Biol.* **128,** 82–97 (1999).
32. Yang, Z., Fang, J., Chittuluru, J., Asturias, F. J. & Penczek, P. A. Iterative stable alignment and clustering of 2D transmission electron microscope images. *Structure* **20,** 237–247 (2012).
33. Hohn, M. *et al.* SPARX, a new environment for cryo-EM image processing. *J. Struct. Biol.* **157,** 47–55 (2007).
34. Mastronarde, D. N. Automated electron microscope tomography using robust prediction of specimen movements. *J. Struct. Biol.* **152,** 36–51 (2005).
35. Brilot, A. F. *et al.* Beam-induced motion of vitrified specimen on holey carbon film. *J. Struct. Biol.* **177,** 630–637 (2012).
36. Campbell, M. G. *et al.* Movies of ice-embedded particles enhance resolution in electron cryo-microscopy. *Structure* **20,** 1823–1828 (2012).
37. Rohou, A. & Grigorieff, N. CTFFIND4: fast and accurate defocus estimation from electron micrographs. *J. Struct. Biol.* **192,** 216–221 (2015).
38. Grant, T. & Grigorieff, N. Measuring the optimal exposure for single particle cryo-EM using a 2.6 Å reconstruction of rotavirus VP6. *eLife* **4,** e06980 (2015).
39. Scheres, S. H. RELION: implementation of a Bayesian approach to cryo-EM structure determination. *J. Struct. Biol.* **180,** 519–530 (2012).
40. Grigorieff, N. FREALIGN: high-resolution refinement of single particle structures. *J. Struct. Biol.* **157,** 117–125 (2007).
41. Gaudet, R. & Wiley, D. C. Structure of the ABC ATPase domain of human TAP1, the transporter associated with antigen processing. *EMBO J.* **20,** 4964–4972 (2001).
42. Eswar, N. *et al.* Comparative protein structure modeling using Modeller. *Curr. Protoc. Bioinformat.* **Chapter 5,** Unit 5.6 (2006).
43. Shintre, C. A. *et al.* Structures of ABCB10, a human ATP-binding cassette transporter in apo- and nucleotide-bound states. *Proc. Natl Acad. Sci. USA* **110,** 9710–9715 (2013).
44. Emsley, P., Lohkamp, B., Scott, W. G. & Cowtan, K. Features and development of Coot. *Acta Crystallogr. D* **66,** 486–501 (2010).
45. DeLano, W. L. The PyMOL molecular graphics system (DeLano Scientific, 2002).
46. Pettersen, E. F. *et al.* UCSF Chimera—a visualization system for exploratory research and analysis. *J. Comput. Chem.* **25,** 1605–1612 (2004).

Extended Data Figure 1 | Cloning strategy for TAP1-protein A/TAP2 co-expression.

Data set #1

692 movies

|
autopick
|

32,228 particles

Data set #2

1524 movies

|
autopick
|

141,164 particles

combine particles

173,392 particles

2D classification

83,815 particles

3D classification

63,621 particles

Data set #3

2947 movies

|
autopick
|

357,654 particles

2D classification

225,727 particles

3D classification

86,158 particles

3D auto-refine

3D classification, no align

75,672 particles

combine particles

139,293 particles

3D auto-refine

FREALIGN

Extended Data Figure 2 | Cryo-EM data processing flowchart.

Extended Data Figure 3 | FSC indicating the resolution of the density map. FSC plots were generated between reconstructions from random halves of the data. The frequency at which the dashed line passes through FSC = 0.143 indicates the reported resolution. Corresponding values are given in Extended Data Table 1.

Extended Data Table 1 | Summary of cryo-EM data

Data collection

Microscope	Titan Krios I, 300 keV (FEI)
Detector	K2 Summit direct electron detector (Gatan)
Pixel size	1.35 Å
Energy filter	20 eV (Gatan)

Dataset # 1

Movies	692
Frames	20
Dose	2.2 electrons/Å^2/frame
Defocus range	-1.6 to -3.0 µm

Dataset # 2

Movies	1524
Frames	40
Dose	2.2 electrons/Å^2/frame
Defocus range	-2.0 to -5.0 µm

Dataset # 3

Movies	2947
Frames	40
Dose	2.2 electrons/Å^2/frame
Defocus range	-1.5 to -3.5 µm

Final Reconstruction

Number of particles	139,293
Accuracy of rotations	2.78 degrees
Accuracy of translations	0.98 pixels
Overall resolution	6.5 Å
B-factor correction	-500 Å^2